



Impact of Assimilated Precipitation-Sensitive Radiances on the NU-WRF Simulation of the West African Monsoon

SARA Q. ZHANG

NASA Goddard Space Flight Center, Greenbelt, Maryland, and Science Applications International Corporation, McLean, Virginia

T. MATSUI

NASA Goddard Space Flight Center, Greenbelt, and Earth System Science Interdisciplinary Center, University of Maryland, College Park, College Park, Maryland

S. CHEUNG

University of California, Davis, Davis, California

M. ZUPANSKI

Cooperative Institute for Research in the Atmosphere, Colorado State University, Fort Collins, Colorado

C. PETERS-LIDARD

NASA Goddard Space Flight Center, Greenbelt, Maryland

(Manuscript received 5 October 2016, in final form 7 June 2017)

ABSTRACT

This work assimilates multisensor precipitation-sensitive microwave radiance observations into a storm-scale NASA Unified Weather Research and Forecasting (NU-WRF) Model simulation of the West African monsoon. The analysis consists of a full description of the atmospheric states and a realistic cloud and precipitation distribution that is consistent with the observed dynamic and physical features. The analysis shows an improved representation of monsoon precipitation and its interaction with dynamics over West Africa. Most significantly, assimilation of precipitation-affected microwave radiance has a positive impact on the distribution of precipitation intensity and also modulates the propagation of cloud precipitation systems associated with the African easterly jet. Using an ensemble-based assimilation technique that allows state-dependent forecast error covariance among dynamical and microphysical variables, this work shows that the assimilation of precipitation-sensitive microwave radiances over the West African monsoon rainband enables initialization of storms. These storms show the characteristics of continental tropical convection that enhance the connection between tropical waves and organized convection systems.

1. Introduction

The precipitation of the West African monsoon (WAM) not only provides vital water resources to the region, but also modulates tropical climate and, potentially, global climate change (Giannini et al. 2008). For a better understanding and prediction capability of the WAM, the scientific community devoted a multidisciplinary analysis in the region (Redelsperger et al. 2006). The features of the WAM are complex with multiscale

interactions between dynamics and precipitation processes. For example, at synoptic time scales, variability of the rainfall is observed linking to tropical wave dynamics (Mounier et al. 2007) and the extratropical intrusion of dry air (Roca et al. 2005). The dominant mode of synoptic variability of precipitation is correlated with African easterly waves (AEWs) through the dynamic relationship to organized convection systems (Kiladis et al. 2006; Skinner and Dickenbaugh 2013).

Satellite observations and numerical model simulations are powerful tools to gain a better understanding of the WAM and the prediction of its future evolution. For

Corresponding author: Sara Q. Zhang, sara.q.zhang@nasa.gov

DOI: 10.1175/MWR-D-16-0389.1

© 2017 American Meteorological Society. For information regarding reuse of this content and general copyright information, consult the [AMS Copyright Policy](http://www.ametsoc.org/PUBSReuseLicenses) (www.ametsoc.org/PUBSReuseLicenses).

example, satellite-based precipitation estimates and ground-based observations from the African Monsoon Multidisciplinary Analysis (AMMA) program are used to examine the monsoon rainfall variability at a range of different time scales (Roca et al. 2010). To investigate the interconnection between dynamics of AEWs and moist processes associated with cloud, precipitation, and deep convection, McCrary et al. (2014) carried out an extensive simulation of the WAM using a super-parameterized climate model. Their simulation demonstrated that AEWs are sensitive not only to model resolution, but also to model moist physics. Their results showed that an improved representation of subgrid-scale cloud precipitation and convection allows AEWs to develop even at a modest coarse resolution, and to maintain spatial structures and temporal variability comparable to observations.

However, the quality of analyses based on observations only is limited by the partial data coverage in space and time, and the lack of cross-variable consistency among individually retrieved quantities. On the other hand, the fidelity of model simulations is affected by the model resolution and parameterized physics schemes, which often results in large uncertainties, especially in precipitation and clouds. There are analysis experiments using data fusion approaches to combine model simulation and precipitation observations. For instance, the Modern-Era Retrospective Analysis for Research and Applications (MERRA) product used so-called post-analysis adjustment on the surface precipitation field, which adjusts precipitation produced from model forecasts to fit available precipitation retrievals (Bosilovich et al. 2011). Although this approach produces better surface precipitation analysis, it does not directly provide a better representation of the interaction and feedback of the precipitation to model thermodynamics and meteorological conditions. To correct for this disconnection between precipitation and thermodynamic fields, a new WAM analysis is needed that assimilates observations interactively into model simulation to constrain the model representation of dynamics and physical processes. An example of recent development and experiment in this direction is the NASA Goddard Earth Observing System, version 5 (GEOS-5), reanalysis that assimilates aerosol optical depth from satellite passive visible imagers into the global GCM with interactive radiative impact of aerosols. The product provides continuous spatial distributions of aerosols consistent with the satellite observations, which allows a more realistic investigation on the African easterly jet (AEJ) (Reale et al. 2011, 2014).

This work advances to assimilate precipitation-sensitive radiances into high-resolution mesoscale

atmospheric simulations of the WAM. The goal is to create cloud and precipitation distributions that are consistent with satellite observations and physical constraints of the underlying processes, with fully realized dynamic interaction and feedback through explicit microphysics and mesoscale dynamics. Using an advanced ensemble data assimilation system developed for the NASA Unified Weather Research and Forecasting (NU-WRF; Peters-Lidard et al. 2015) Model, precipitation-sensitive microwave radiances are directly assimilated into a storm-scale NU-WRF simulation of the WAM. Assimilation of precipitation-affected radiance data into numerical weather prediction models has been shown to improve the simulations of precipitation and underlying thermodynamic processes. The European Centre for Medium-Range Weather Forecasts (ECMWF) system routinely assimilates all-sky microwave radiance observations in its global numeric weather prediction system and found a positive impact on the accuracy of analysis and forecast skills (Geer et al. 2010; Geer and Bauer 2011). Assimilation of Global Precipitation Measurement (GPM) data into a regional WRF simulation of storms over midlatitude continents improved spatial distributions of precipitation in the analyses and short-term forecasts (Zhang et al. 2013; Chambon et al. 2014). Even though the African continental environment is challenging to all-sky radiance assimilation, we anticipate that the simulation of the WAM would be improved by incorporating satellite observations on precipitation processes. With integration of available information by an ensemble-based data assimilation system, the analysis can provide a multiscale description of monsoon precipitation and consistent dynamics of the WAM.

The experiment in this work assimilates microwave radiance observations from multiple spaceborne passive microwave sensors under precipitating and cloudy conditions with the NU-WRF framework, and evaluates the data impact against independent observations. Because of the computational cost of high-resolution ensemble data assimilation, the experiments are carried out in a relative short period of 7 days during WAM season. Section 2 provides an overview of the model and data assimilation system. Section 3 describes the experiment configuration, the microwave radiances assimilated in the experiment, and independent data used for verification, followed by the presentation and discussion of the results in section 4. A summary of this study is given in section 5.

2. NU-WRF Ensemble Data Assimilation System

NU-WRF is an observation-driven integrated modeling system that represents cloud, precipitation,

aerosol, and land process (Peters-Lidard et al. 2015). It is based on the Advanced Research WRF (Skamarock et al. 2008) with additional coupling to advanced Goddard physics packages, satellite simulators, and high-resolution satellite/reanalysis data to initialize boundary conditions. In this work the NU-WRF model simulations are carried out at storm scale with lateral boundary forcing from the Modern-Era Retrospective Analysis for Research and Applications, version 2 (MERRA2; Gelaro et al. 2017). The NASA Land Information System (LIS) (Peters-Lidard et al. 2007) provides observation-corrected land surface conditions.

Because remote-sensed passive microwave measurements respond directly to scattering optical properties of precipitating particles in the atmosphere, rather than to surface precipitation amounts, the microphysics in the model is a crucial component for the application of radiance-based precipitation and cloud data assimilation. Goddard microphysics schemes (Lang et al. 2011) explicitly resolve the evolution of microphysical variables, which enables the data assimilation system to include hydrometeor distributions in the control vector.

The NU-WRF Ensemble Data Assimilation System (NU-WRF EDAS) is developed to produce regional analyses and forecasts at high resolution. The key feature of this data assimilation system is that microwave radiances in cloudy and precipitating areas are directly assimilated along with conventional observations and other satellite data types in clear-sky regions (Zhang et al. 2013). The assimilation of satellite precipitation data provides important information on physical processes and constrains cloud and precipitation where model simulation is often subject to substantial forecasting errors. The satellite simulator connects the all-sky states of forecast model to the microwave-observable brightness temperature (Matsui et al. 2014). The analysis control variables are wind, temperature, surface pressure, water vapor, and prognostic cloud and precipitation in frozen and liquid phases. An ensemble of NU-WRF forecasts is used to calculate state-dependent background error covariance, and a maximum likelihood ensemble filter solves the analysis problem (Zupanski 2005). The ensemble innovation covariance is calculated to project information between control variable space and observation space, without a need of tangent linear and adjoint models for the non-linear observation operator.

The evolution and distribution of hydrometeors and the corresponding forecast uncertainties are crucial information in assimilating precipitation observations. The high variability and low predictability of precipitation systems requires heterogeneous and flow-dependent background error covariance,

particularly when the prognostic hydrometeors are included in the analysis control vector. The ensemble spread around the central forecast represents the model forecast uncertainty. For example, in a case of storm reintensification after landfall examined in Zhang et al. (2013), there is significant ensemble spread in the distribution and amount of ice-phased hydrometeors above freezing level in the simulation of a storm. Using ensemble forecasts in flow-dependent background error estimation, the background error variances are much larger in the storm region than that in clear-sky area, not only in hydrometeors, but also in the water vapor and temperature fields. This error information will potentially allow more corrections from available observations in the area during the data assimilation procedure. The ensemble-based, flow-dependent forecast error covariance is updated in each data assimilation cycle. Because the cross correlations between the microphysical variables and model dynamical variables are represented in the forecast error covariance as generated from ensemble model forecasts, they are flow-dependent and reflect the dynamical and physical relationship described by the model, allowing a dynamically balanced precipitation analysis. Consequentially, the information in precipitation data would propagate into analysis of other variables and interact with model dynamics. Since the error covariance based on ensemble forecasts can be noisy with a relatively small ensemble size, localization schemes are applied to filter the noise through the weight-interpolation method (Yang et al. 2009). The interpolation is applied to control variables in ensemble space, not to the weight coefficients.

3. Experiments

a. Experiment specifications

The NU-WRF experiments in this study are designed to examine the impact of assimilation of precipitation-affected radiances on the simulation of the WAM. The experiment period of 9–16 August 2006 is after the WAM onset during the NASA African Monsoon Multidisciplinary Analysis (NAMMA) observing campaign. In this period, frequent precipitation systems occurred in a range of scales and characteristics.

The experiment domain is set in the continental West Africa region (5°S–27°N, 20°W–30°E), with horizontal grid spacing of 9 km, and 51 vertical levels from the Earth surface to the top atmosphere level set at 50 hPa. The data assimilation cycling is initialized at 0000 UTC 9 August 2006, with a 3-h assimilation window. The initial perturbations to the 32 ensemble forecasts are generated from an error covariance based on

time-lagged forecasts, and the global reanalysis MERRA2 is interpolated to the resolution of the domain as the atmospheric initial condition. Land surface initial conditions (soil moisture and skin temperature) are derived from LIS spinup (Kumar et al. 2008) of the Noah land surface model (LSM) with the MERRA-Land meteorological forcing (Reichle 2012). In subsequent data assimilation cycles, the analysis produced by assimilating observations is used to issue ensemble 3-h forecasts, with new perturbations derived from updated analysis error covariance. The ensemble forecasts are used to update the forecast error covariance and provide background states to forward models for simulating satellite-observable signals. We conduct two experiments with the configuration described above. The radiance-assimilation run (RADAS) assimilates precipitation-affected radiances along with conventional data. A data-denial run serves as the control (CONTR) without assimilating observations of precipitation-affected radiances. In addition to the two assimilation runs, we also carry out a model simulation at 3 km of horizontal grid spacing without data assimilation (SIMU3KM) for comparison study on the influence of model resolution to the simulated WAM precipitation and the interaction between small-scale processes and large-scale dynamics. All experiments use Goddard 3ICE microphysics (Lang et al. 2011) and Goddard radiation schemes (Chou and Suarez 1999 and 2001). The cumulus parameterization Grell 3D Ensemble scheme (Grell and Devenyi 2002) is used both in 9-km and 3-km resolution simulations.

b. Observations used in assimilation experiments

Precipitation-sensitive microwave radiances are the most prominent data to be assimilated in this study. The NASA Precipitation Processing System (PPS) intercalibrates and manages microwave measurements from a constellation of satellites including the Tropical Rainfall Measuring Mission (TRMM) (Simpson et al. 1996) and Global Precipitation Measurement (GPM) mission (Hou et al. 2014). During the period of this study of the WAM, passive microwave data from six satellites are available. All observations are TRMM constellation cross-calibrated radiances (Level-1C) at sensor native sampling resolutions. The data include measurements from the TRMM Microwave Imager (TMI), Special Sensor Microwave Imager/Sounder (SSMIS) on board the Defense Meteorological Satellite Program (DMSP) F16, Special Sensor Microwave Imager (SSM/I) on board DMSP F13, F14, and F15, and Advanced Microwave Scanning Radiometer for Earth Observing System (AMSR-E) on board the *Aqua* satellite. All instruments use conical scanning system with vertical and horizontal

polarization. The spatial sampling resolutions vary with the channel wavelength in different sensors. For instance the TMI high-frequency channel at 85 GHz has finer resolution ($4\text{ km} \times 6\text{ km}$) of field of view (FOV). These datasets are obtained from NASA PPS GPM/TRMM and Partner Data Archive (pps.gsfc.nasa.gov/).

To directly assimilate precipitation-sensitive radiance data, satellite microwave observations need to be simulated from model states. An all-sky radiative transfer model is applied as the observation operator based on the Goddard Satellite Data Simulator Units (G-SDSU; Matsui et al. 2014). The microwave simulator consists of two-stream radiative transfer calculations with Eddington's second approximation along the slant radiance path (Kummerow et al. 2001; Olson et al. 2006), the TELSEM (Tool to Estimate Land-Surface Emissivities at Microwave Frequencies) atlas (Aires et al. 2011) for land surface emissivity, single-scattering integration, and sensor antenna gain function (Matsui et al. 2013). Antenna gain functions of each instrument are incorporated with respect to the model grid and effective field of view (EFOV). The particle single scattering is calculated through Mie and Maxwell Garnet methods by integrating the particle size distribution, effective density, and different phase consistent to those of Goddard 3ICE microphysics.

Because the experiment domain is mainly over land surface, we rely on high-frequency channels for their sensitivity to ice-phased precipitation (i.e., snow aggregate and graupel) and relative insensitivity to land surface emissivity. Low-frequency channels of 19 and 21 GHz in vertical polarization are added to the calculation of the scattering index over land (SIL) to detect precipitating conditions (Wilheit et al. 2003). Statistical calculations for bias correction and observation errors are based on a longer period of SSMIS data collection (Chambon et al. 2014). In the experiment RADAS, the data selection for TMI, SSM/I, SSMIS, and AMSR-E are based on the SIL of observation and first-guess data. The data selection takes a sampling approach that observations are selected if observation or forecast indicates precipitation condition, which includes three scenarios: 1) both observation and forecast have precipitation, 2) observation detects precipitation, but forecast has no precipitation, and 3) observation is clear sky, but forecast has precipitation. The data are not selected only if both observation and forecast agree in clear-sky conditions (no scattering signal in presence). The data from these instruments are not used in CONTR. The observation error standard deviations are prescribed with consideration of precipitation scenarios, particularly over where the observations and model detect precipitation conditions differently. Table 1

TABLE 1. Microwave level-1 radiance data used in the study; H and V refer to horizontal and vertical polarization, respectively.

Satellite	Instrument	Atmospheric condition	Error std dev (K)	Channels selected for assimilation (field of view resolution)	Channels used in scattering index over land
DMSP F16	SSMIS	Cloudy, precipitation	18	91.6 H (14 km \times 13 km)	19.3 V
			18	91.6 V (14 km \times 13 km)	22.2 V
			18	150.0 H (14 km \times 13 km)	
			16	183.3 \pm 7 H (14 km \times 13 km)	
DMSP F13	SSM/I	Same as above	18	85.5 H (16 km \times 11 km)	Same as above
			18	85.5 V (16 km \times 11 km)	
DMSP F15	SSM/I	Same as above	18	Same as above	Same as above
Aqua	AMSR-E	Same as above	18	89.0 H (6 km \times 4 km)	18.7 V
			16	89.0 V (6 km \times 4 km)	23.8 V
TRMM	TMI	Same as above	18	85.0 H (7 km \times 5 km)	19.3 V
			16	85.0 V (7 km \times 5 km)	21.3 V

summarizes the information on observations assimilated in the experiments, including the channels, resolutions, and observation errors under precipitation conditions. The online quality control criteria for precipitation-affected radiance are observation departure < 50 K and SIL > 10 K for either observations or first guess. Data that have FOV over mixed sea and land surface are not used. Since the size of observation FOV is comparable to the model spatial resolution in this experiment, data thinning is not applied to these high-frequency radiance observations. The possibility of correlated observation errors in radiance space still exists, though it will be much less likely than using retrieved products. The radiance observation error covariance is set to be diagonal in this study. Because this is regional data assimilation, the data counts vary from time to time depending on the satellite track covering the domain and the resolution of the instrument.

Traditional global analyses from operational systems are used to initialize the ensemble forecasts at the initial data assimilation cycling period. The large-scale forcing for subsequent forecasts during the cycling period is applied through domain boundaries. To constrain the dynamical forcing in domain interiors, the following data from the operational global observing system are also assimilated: in situ conventional observations and clear-sky radiances from temperature and moisture-sensitive channels of Advanced Microwave Sounding Unit A (AMSU-A) and Unit B (AMSU-B). These datasets are obtained from UCAR/NCAR Research Data Archive (rda.ucar.edu/).

In addition to the radiances and the ground-based conventional data, independent observations are used to evaluate the impact of data assimilation to the simulation of the WAM. In this study we utilize independent observations from TRMM Precipitation Radar (PR), TRMM multisensor retrieved surface rain rates (TRMM level-3 product), geostationary infrared (IR)

brightness temperature Tb, and *CloudSat* Cloud Profiling Radar (CPR). More detailed descriptions on these datasets are provided in the next section.

4. Results

a. Microwave radiances and hydrometeors

An effective assimilation of spaceborne indirect observations such as radiances is expected to produce corrections on model control variables that are physically related to the observed quantities. Therefore, the error reductions measured in precipitation-sensitive radiance departures represent a better agreement between hydrometeors in corresponding analysis with the observed. The time series of the root-mean-square error (RMSE) of radiance departures presented in Fig. 1 is an overall evaluation on the effectiveness of radiance data

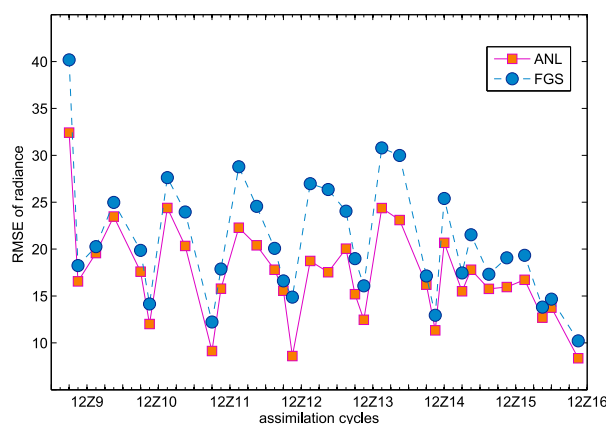


FIG. 1. RMSE of radiance departures (in K) during the data assimilation cycling period. Cycle 1 corresponds to the analysis time at 0300 UTC 9 Aug 2016. The assimilation window is 3 h, and departure samples are collected from precipitation-sensitive channels of all microwave sensors assimilated: the first-guess departures are in blue and analysis departures in orange.

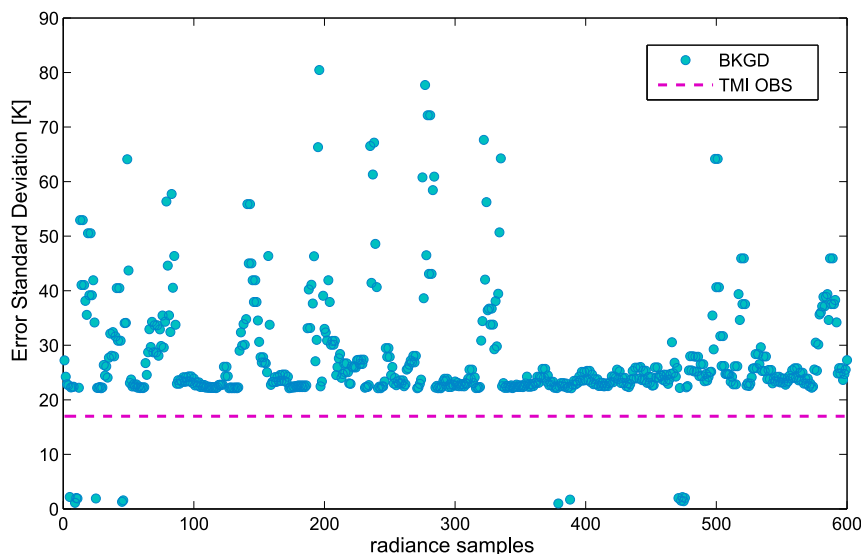


FIG. 2. Standard deviations of the ensemble spread in radiance space sampled at TMI 85-GHz observation locations at analysis time 1500 UTC 12 Aug 2016. The prescribed observation error standard deviation is represented by the dashed line.

assimilation. The error statistics are calculated based on data of all precipitation-sensitive channels. The assimilation procedure is performed at each analysis time in ensemble space. The result is projected in observation space as minimized departures between the observed and simulated radiances. As shown in Fig. 1, comparing the first-guess departure (blue) to the analysis departure (orange), the discrepancies between the observed and model-simulated radiances are reduced when observations are available in the model domain.

Effectiveness of assimilating precipitation-sensitive radiances depends on the error information provided by background and observation error covariance. The ratio of background errors and observation errors in radiance space in data assimilation is similar to the signal-to-noise ratio in measure of information content (Rodgers 2000). For instance, if background error projected in radiance space is too small relative to observations error, assimilation procedures will not be able to effectively extract information from observations to produce analysis increments (Zupanski et al. 2007). In this ensemble data assimilation system the background error covariance is state-dependent and so is the projection from state space to radiance space. Hence the ratio of the errors in radiance space varies spatially and temporally during the assimilation cycling. The ensemble spread in radiance space can represent background uncertainty projected in observation space. In each analysis cycle the ensemble forecasts are issued from initial conditions that are perturbed according to previous analysis error covariance. The background states

are inputted to the all-sky radiance transfer model to obtain an ensemble of simulated radiance fields. Then the ensemble spread is calculated at available observation locations. Figure 2 shows an example of standard deviations of the ensemble spread in radiance space comparing to the radiance observation errors, sampled from one analysis time (1500 UTC 12 August 2016) when TMI 85-GHz observations are assimilated. On average the ratio of background and observation errors is in the range of 1.5–2.0 under cloudy and precipitating condition, indicating that signal is relatively larger than noise, the assimilation procedure can extract observation information effectively.

The cumulative distribution of observed Tb is associated with the occurrence of precipitation intensity distribution (Matsui et al. 2009). For example, if considerable occurrences of Tb depression are observed in high-frequency channels over land, substantial occurrence of deep-convective precipitation events can be inferred to have a similar probability distribution. Figure 3 compares the cumulative probability density of observed and the simulated Tb TMI 85 GHz(V), sampled from all TMI overpasses during the experiment period. The distribution of observations (in blue) has significant occurrences of large Tb depression below 240 K, indicating that they represent rather frequent heavy rainfall and convective storms. This is due to the signal's strong sensitivity to the presence of frozen precipitation aloft that is associated with deep convection. The simulated Tb from CONTR (in green) manifests underestimation of the frequency and intensity of such

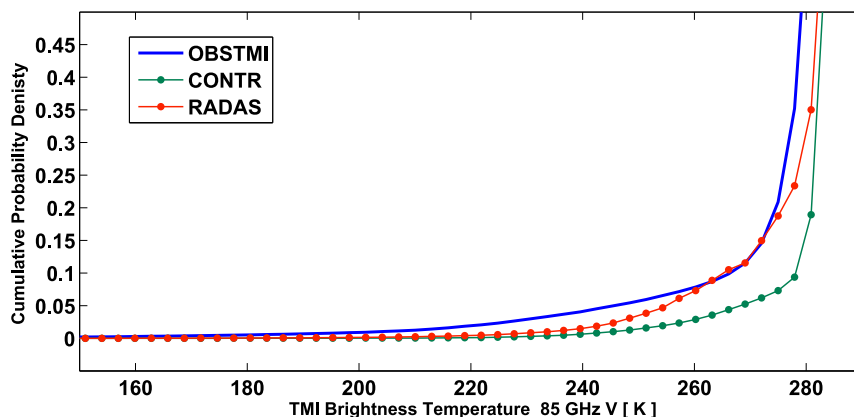


FIG. 3. The cumulative probability density of the radiances in TMI 85 GHz (V). Observations are collected from TMI overpasses in the domain during the experiment period. Simulated radiances are in green and red (from CONTR and RADAS, respectively).

precipitation events. Assimilation of precipitation-sensitive radiances from RADAS (in red) improved the Tb distributions closer to the observed one, suggesting the improvement of occurrence and intensity of the precipitation of the WAM.

It has been observed that convective storms are frequently initiated by unstable atmospheric conditions in regions with varied surface conditions such as large gradients in soil moisture and skin temperature during the WAM (Wu et al. 2009). However, the initiation and evolution of these convective-related geophysical systems are difficult to simulate by forecast models, even at storm-permitting resolution (Roehrig et al. 2013;

McCrary et al. 2014). By the virtue of assimilating precipitation-sensitive radiance, the analysis may provide the model with initial conditions that are favorable to start convective processes. An illustrative case is presented here chosen from the best available results. A storm near the west coast in the WAM region was observed by TRMM satellite overpass on 0600 UTC 13 August 2016, shown in Fig. 4. The deep Tb depression in TMI high-frequency channel 85-GHz observations indicates that a large amount of frozen precipitating particles aloft. The TRMM PR reflectivity observations also confirm the convective vertical distribution of precipitating particles. However, the model

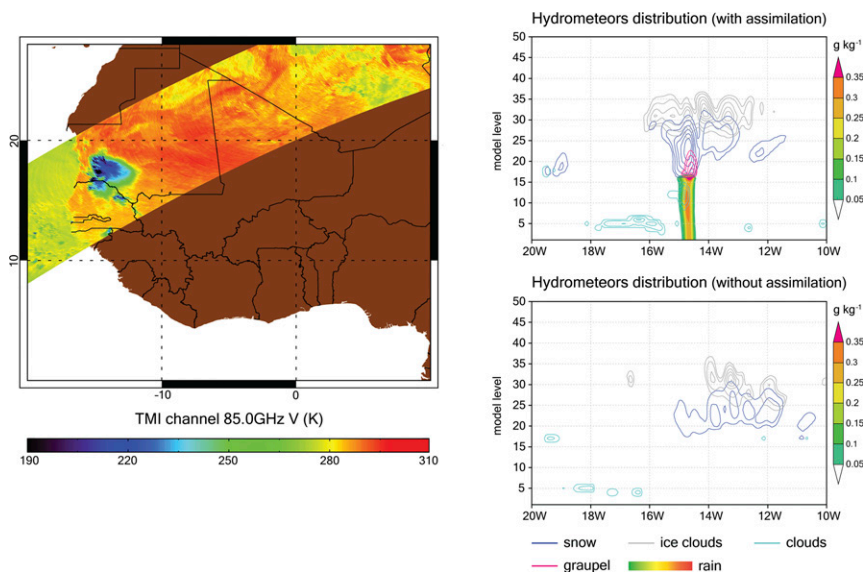


FIG. 4. The storm observed from space by TRMM TMI, at 0600 UTC 13 Aug 2006, (left) as Tb depression (in blue shade) in the 85-GHz (V) TMI channel. (right) The hydrometeors in the atmosphere (in g kg^{-1}), in vertical–zonal cross section in the storm area (17°N), (top) with and (bottom) without precipitation-sensitive radiance assimilation, respectively.

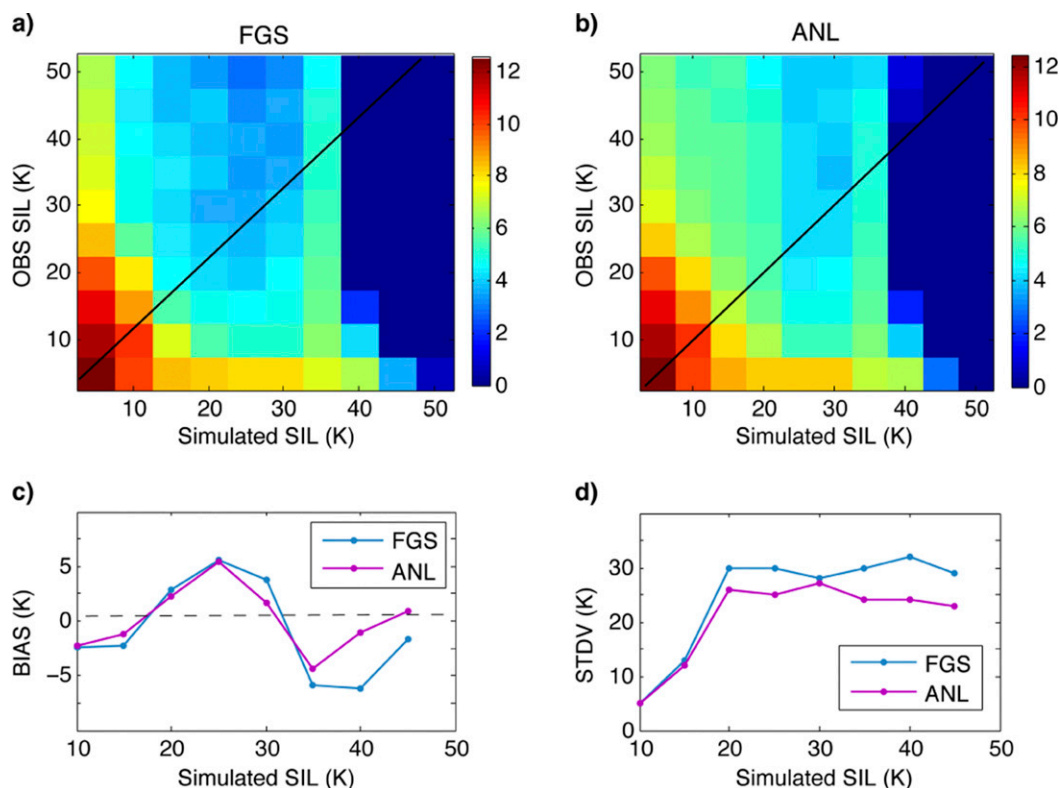


FIG. 5. (top) 2D histogram of radiance departure sample counts, segregated by the scattering index of over land (SIL). The departures are sampled from observed and simulated TMI 85 GHz in all TMI overpasses in the domain during the experiment period. The SIL indices are calculated from observations (vertical axis) and from simulations (horizontal axis). The color shades represent departure sample counts (in log scale): (a) for FGS and (b) for ANL as before and after analysis, respectively. (bottom) As in (top), but for (c) biases and (d) error standard deviations, calculated from the departure samples, binned by averaged observation and simulation SIL.

simulation without radiance assimilation (CONTR) has few clouds and negligible precipitation in the area as shown in the bottom right panel of Fig. 4. In contrast, a coherent distribution of hydrometeors (precipitation and cloud) is established by assimilation of TMI radiance observations (RADAS), as shown in the top right panel of Fig. 4. Among the control variables, most sensitive hydrometeor to TMI high-frequency Tb is the ice-phased precipitation above freezing level illustrated in blue contours. The cross-covariance in the ensemble-estimated forecast error covariance is based on cloud physics that provides a physically based correlation among hydrometeors that support the convective storm structure. As demonstrated in this case, rainfall is below freezing level (in colored shades), mixed-phase precipitation is in the middle (in orange contours), and cloud distribution is associated with detrainment (in dashed blue contours).

A long-standing challenge of model precipitation simulation is the location or phase error of precipitation systems, and it becomes more outstanding when the

model resolutions become finer. These model errors appear in data assimilation systems as biases in observation departure statistics. In NU-WRF EDAS radiance observations samplings are categorized by the scattering index criterion as precipitation-affected or non-precipitating pixels. A so-called symmetric sampling method is applied to include any observation departure (observation minus first guess) sample where precipitation is detected either by observation or by model simulation (Zhang et al. 2013). Figure 5 presents a pair of radiance observation departure 2D histograms that bin the departure samples according to scattering index values calculated from observations and from simulations. The color shades of the histogram represent sample counts (in log scale) in each bin. The observation departures are Tb TMI 85 GHz collected from all TMI overpasses during the experiment period. The samples, located at the far left column in the histogram, show that precipitation is detected by observation (with large scattering index value toward the upper left corner) but missed by the model (with scattering index smaller than

10 K). The opposite situation is represented by the samples located in the bottom row. In a perfect forecast scenario all samples would be on the diagonal. The comparison of the histograms of before (FGS) and after analysis (ANL) of radiance departures shows that the radiance assimilation increases the sample counts in the bins closer to the diagonal line, which indicates more samples have smaller discrepancy on scattering strength between the observed data and what is simulated after analysis. Note that the scattering signals of observations do not change; only the signals of the simulations change, mainly from analysis corrections on hydrometeors. The analysis impact is represented by the migration of samples toward the diagonal line of the histogram. The model biases from dislocation or phase error of precipitation yet remain in the analysis, as represented by the sample counts on the far left column and the bottom row of the ANL histogram. The bias and the error standard deviation are calculated from the departure samples of FGS and ANL as a function of averaged SIL (observation and simulation). The comparisons of the statistics are shown in the lower left panel (biases) and the lower right panel (error standard deviations) in Fig. 5. They confirm that the analysis effectively reduces the discrepancy between model simulation and observation within the limitation of present model biases and possible forward model biases.

b. Surface precipitation

Improving the model-simulated precipitation of the WAM is a critical goal of assimilating satellite observations in precipitation regions. Whenever observations are available, the observation information is assimilated into model initial conditions such as hydrometeor distributions, moisture, and temperature profiles. The model is initialized from those initial conditions and produces short-term forecasts of surface rainfall dynamically consistent with the environment. We will use a combined-observation rain retrieval product to assess precipitation fields from subsequent short-term forecasts issued by CONTR and RADAS. The TRMM 3B42 product is surface precipitation rate retrieval by the GPROF algorithm (Kummerow et al. 2001). In the TRMM satellite observed region, surface rain rates are retrieved based on the database from TMI with additional information from independent observations of TRMM PR, ground-based rain gauge analyses, and microwave-calibrated infrared data (Huffman et al. 2007; Kidd et al. 2003). The data are merged to a 0.25° grid and 3-hourly average. The dataset is obtained from NASA PPS TRMM Multisatellite Precipitation Analyses data archive (pps.gsfc.nasa.gov). Extensive validation efforts were conducted to compare TRMM 3B42

rain estimates with ground-based rain estimates. In particular, consistent agreement was found at the 1° daily scale with rain gauge data over West Africa (Roca et al. 2010).

First, we present an example on how the assimilated radiance observations affect the subsequent short-term surface precipitation forecasts. On 10 August around the time of 2100 UTC, an overpass of SSM/I on board satellite *F15* observed storms in Nigeria and the surrounding region. Figure 6 shows the deep Tb depression (SSM/I 85 GHz) in the storm area. These precipitation-affected radiance observations are assimilated in RADAS at the analysis time of 2100 UTC. Subsequently two 3-h forecasts are issued, one from RADAS analysis and the other from CONTR. Comparing the two surface rainfall results shown in this case, it is evident that the RADAS-initiated precipitation forecast particularly its spatial pattern is directly related to the radiance assimilation. The precipitation amount and location of the storm is better forecasted by RADAS than by CONTR. The spatial correlation coefficients between the Tb depression and the accumulated precipitation shown in Fig. 6 are -0.34 and -0.18 for RADAS and CONTR, respectively. The correlations are statistically significant with null hypothesis test probability less than 10^{-4} . This is an indirect verification that observation impact is realized and sustained in this short-term storm forecast.

The accumulated surface precipitation in the entire domain during the experiment period is shown in Fig. 7. The observation rainfall shows maxima in the coastal region of Guinea and in the rainband between 10° and 12°N , associated with the intertropical convergence zone (ITCZ) location of the season. The spatial distribution of accumulated surface precipitation from RADAS has a good agreement with the observed in terms of maxima and rainband center locations, as shown in the upper-right panel. The corrections relative to CONTR are mostly made locally on rainfall magnitudes or location shifts (not shown). The statistics calculated against observations shows that model simulated the WAM precipitation from both RADAS and CONTR have positive biases of 9 and 5 mm in the west coastal region, and underestimate the rain amount in the adjacent area to the east. The model precipitation local maximum concentrates near the coastline. The rain spatial coverage does not spread as far inland as in the observations. It may be caused by the nonlinear interaction of model dynamics and microphysics in the transition zone from ocean to land surface. The forward model for microwave radiance assimilation has large uncertainty in simulating radiance with mixed sea and land surface. Therefore RADAS rejects radiance observations along coastlines. The comparison of the zonal

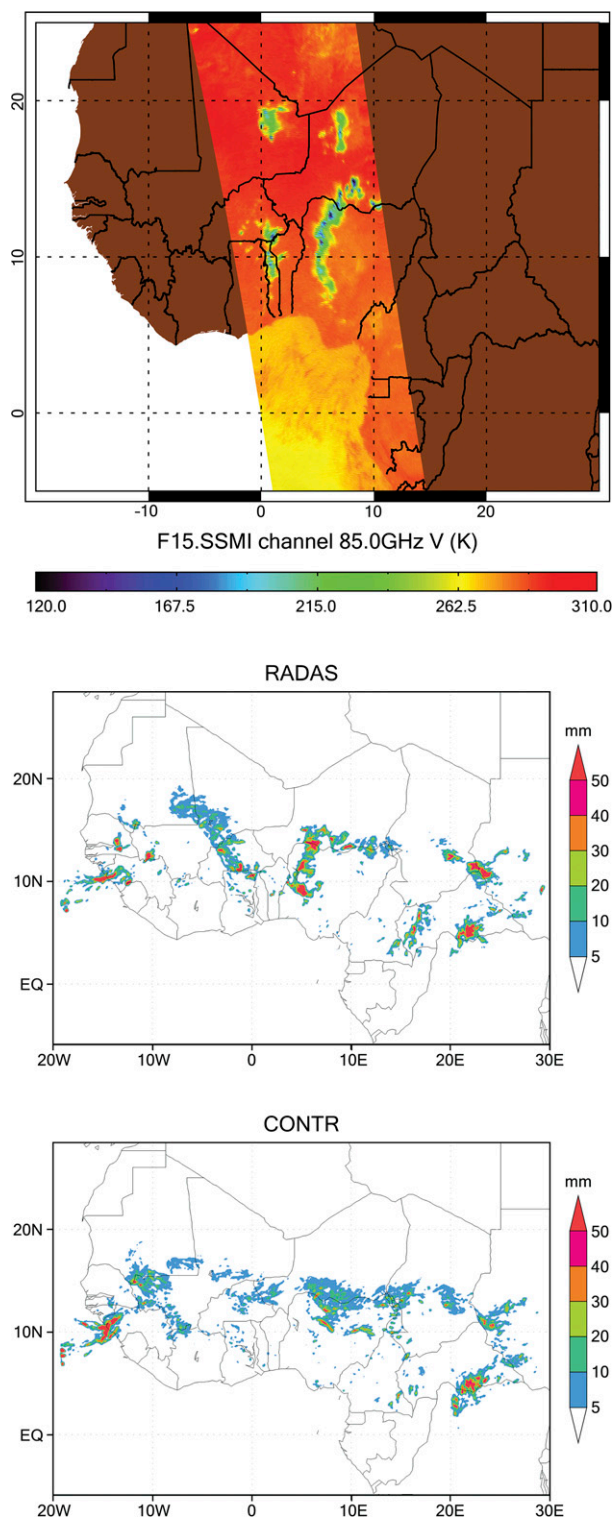


FIG. 6. (top) An overpass of SSM/I at 2100 UTC 10 Aug 2006 observed the precipitation systems in SSM/I channel 85 GHz (in K). The radiance observations are assimilated at the analysis time in RADAS. (middle) Subsequent 3-h model forecast of surface rainfall accumulated from 2100 UTC 10 Aug to 0000 UTC 11 Aug 2006 (in mm). (bottom) Surface precipitation forecast in the same period without data assimilation.

mean accumulated precipitation is presented in Fig. 7 (lower-left panel). Both RADAS and CONTR produce the monsoon rainband center location closely to that of observed. RADAS has better agreement to the observations in terms of precipitation amount in the entire rainband than that of CONTR. The diurnal cycle of monsoon rainfall is examined using 7-day surface precipitation fields from RADAS and CONTR. Figure 7 (lower-right panel) also depicts the comparison of precipitation diurnal cycle. Comparing to the observations, the model rain diurnal cycle has a good agreement with observations on the timing of increasing precipitation in the morning hours. For the late afternoon precipitation, CONTR peaks earlier than observations and falls earlier as well. RADAS has a peak time and duration similar to that of observations, although the magnitudes are lower than the observed.

It is well recognized that high-resolution precipitation forecasts often score poorly when verified using traditional point-to-point comparison metrics because of the low predictability of a convective-scale system with an exact match to the observations at high resolution. As we described in the previous section, radiance observation departures contain predominant biases caused by mismatches because the departures are calculated by point-to-point comparisons. We will use one of the fuzzy verification approaches named the fractions skill score (FSS) to evaluate model simulated surface precipitation of the WAM from CONTR and RADAS at multiple spatial scales. FSS compares the fractional coverage of events in windows surrounding the observations and forecasts. The forecast is measured if the frequency of forecast events is similar to the frequency of observed events: the perfect match scores 1 and nonoverlap scores 0 (Roberts and Lean 2008; Ebert 2008). We calculate FSS scores from precipitation of RADAS and CONTR verified by TRMM 3B42 observations. Figure 8 lists the scores of RADAS and an improvement/degradation matrix from comparison of the scores of RADAS to that of CONTR. The scores reveal different levels of forecast accuracy depending on the scale and intensity. FSS increases with increasing scale as the forecast and observed probabilities became more similar, and it decreases with the increasing rain intensity thresholds when the probability of heavy rain events are relatively low. The assimilation of radiance has modest but positive influence on the precipitation forecast skills across the scales for rain rate less than 60 mm day^{-1} . Both experiments have low scores in the regime of intense rain rates. RADAS has less skill comparatively; it has more frequent heavy rain events than CONTR and the observed in the range of $90\text{--}110 \text{ mm day}^{-1}$. This could be caused by the model physics overreacting to the

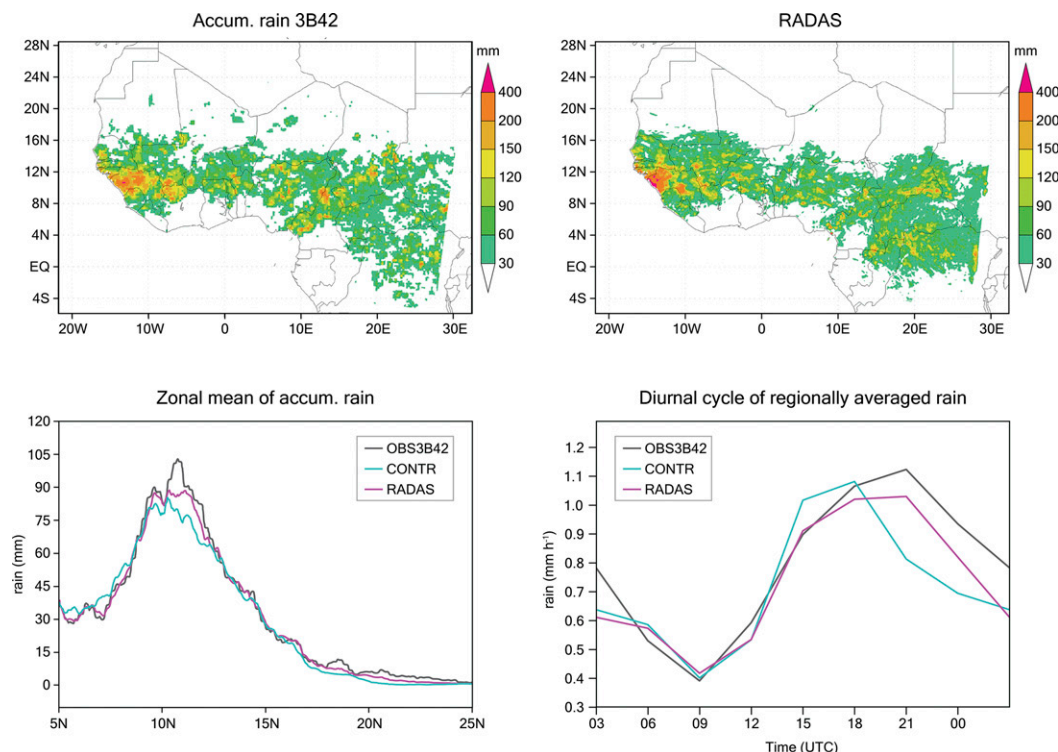


FIG. 7. The accumulated surface precipitation (in mm) in the domain during the experiment period. (top left) The rain estimate of TRMM 3B42, (top right) the surface precipitation from RADAS, (bottom left) the zonal mean comparison among RADAS, CONTR, and TRMM 3B42, and (bottom right) the comparison in terms of diurnal cycle.

precipitation analysis increments by producing more intense rainfall than the observed. There is also an issue of systematic biases in the radiative transfer model. For instance, the TMI 85-GHz probability density

distribution in Fig. 3 shows underestimation of brightness temperature depressions in simulated radiances. The TMI 85-GHz departure 2D histogram in Fig. 5 exhibits asymmetric distribution of the departure samples

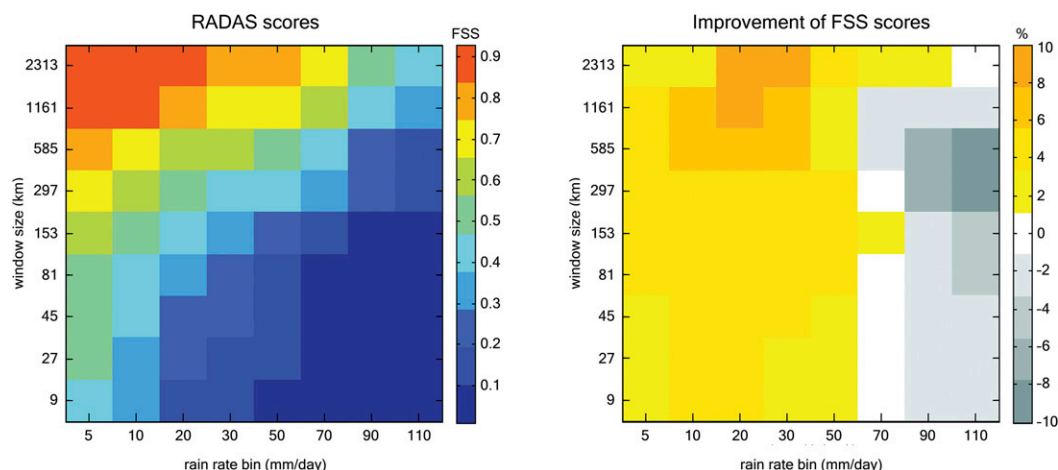


FIG. 8. Fractions skill score (FSS) matrix calculated from model-simulated surface precipitation with TRMM rain estimates 3B42 product as verification. (left) The FSS matrix for RADAS, with perfect match scores 1 and non-overlap scores 0. (right) A relative improvement/degradation matrix is calculated from FSS of RADAS and CONTR.

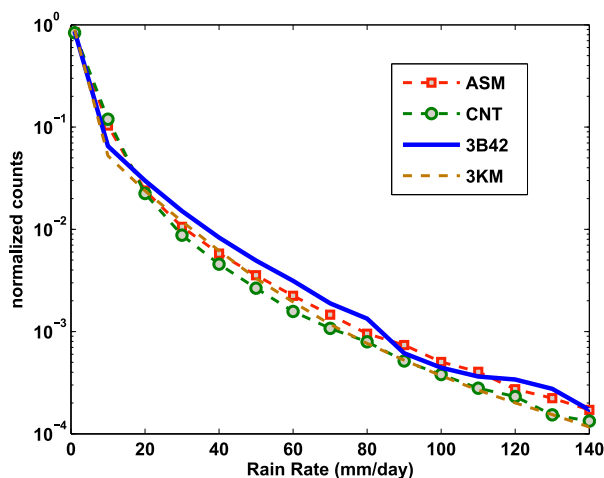


FIG. 9. The probability distribution of surface rain intensity. Data are collected from the rain estimates of TRMM 3B42 product, and surface rain rates produced in short-term 3-h forecasts from CONTR and RADAS in the domain.

indicating that the forward model may have a warm bias in Tb simulation in presence of strong scattering. The current scattering particle shape for ice-phased precipitation is approximated as a soft sphere with constant density. This approximation can cause systematic underestimation of scattering that leads to warm biases in simulated brightness temperature (Olson et al. 2016). The warm biases in simulated radiance could cause analysis biases with larger analysis increments to induce intense rainfall.

The probability of the occurrence of precipitation, regardless of location or phase, is another important measure for detecting model physics bias, and systematic changes of the WAM in climate studies. This statistical evaluation focuses on the probability distribution of precipitation intensity and frequency when compared to that of observations. We examine the probability distribution of precipitation intensity from both experiments. Observed and simulated surface daily rain rates are sampled in the domain in the entire experiment period. Figure 9 plots the normalized histogram with daily rain rates binned from very light to heavy rainfall. Verified against the observations, the assimilation experiment result of RADAS improved rain intensity distribution consistently across a range of rain rates. There is not noticeable change in light rain regime.

c. Cloud distribution and evolution

Cloud processes play a very important role in the complex connection and feedback between physical processes and large-scale dynamics in the WAM. Assimilation of precipitation-sensitive radiances impacts

the horizontal and vertical distribution of clouds as well as the temporal evolution. For instance more frequent convective storms may be associated with a larger population of high-top clouds, which in turn may correspond to a lower outgoing longwave radiation.

We use a high-resolution infrared radiance dataset from merged geostationary satellites to examine whether the precipitation data information influences the model simulated cloud processes in the WAM. The merged IR Tb product is a globally merged observation dataset formed from the $\sim 11\text{-}\mu\text{m}$ IR channels aboard the *GMS-5*, *GOES-8*, *GOES-10*, *Meteosat-7*, and *Meteosat-5* geostationary satellites. It has 4-km spatial resolution and half-hour temporal resolution, making the data particularly valuable in analysis of cloud system propagation and evolution (Janowiak et al. 2001).

The model-simulated cloud systems from subsequent short-term forecasts in CONTR and RADAS are evaluated in IR observation space. The observable brightness temperatures ($T_{b11\mu\text{m}}$) are simulated using visible-IR simulator in the G-SDSU (Matsui et al. 2014). The visible-IR simulator consists of a discrete-ordinate radiative transfer scheme (Nakajima and Tanaka 1986), different phase-function calculation (Nakajima and Tanaka 1988), and spectrum IR emissivity database (Seemann et al. 2008). The inputs to the radiative transfer calculation include environmental information such as thermodynamic state and hydrometeor distribution, as well as the land surface variables. The cloud systems and land surface temperature are depicted in $T_{b11\mu\text{m}}$ space corresponding to cloudy or clear-sky conditions, respectively. Typically in this environment, high Tb ($>280\text{ K}$) corresponds to the land surface skin temperature, and lower Tb ($<280\text{ K}$) corresponds to cloud-top temperature. At the low end of spectrum, cold Tb ($<240\text{ K}$) indicates an active convection system. In between, there are representations of cloud-top temperature from mid- and low-level clouds.

The time series of the $T_{b11\mu\text{m}}$ histogram are shown in Fig. 10. This so-called contoured frequency of time series diagram (CFTSD) of $T_{b11\mu\text{m}}$ is designed to depict diurnal cycle of convection spectrum as well as land surface skin temperature (Matsui et al. 2014). The observations show that maximum $T_{b11\mu\text{m}}$ peaks at local solar noon (1200 UTC). After sunset (1800 UTC), it decreases slowly by radiative cooling until the next sunrise. The occurrence of lower $T_{b11\mu\text{m}}$ started to increase around 1800 UTC, approximately 6 h after the peak of the surface temperature, suggesting the buildup of deep clouds and cirrus anvils during the late afternoon. The cloudiness gradually decreased to minimum in the early morning. RADAS simulation captures the basic feature of observed $T_{b11\mu\text{m}}$ CFTSD, namely

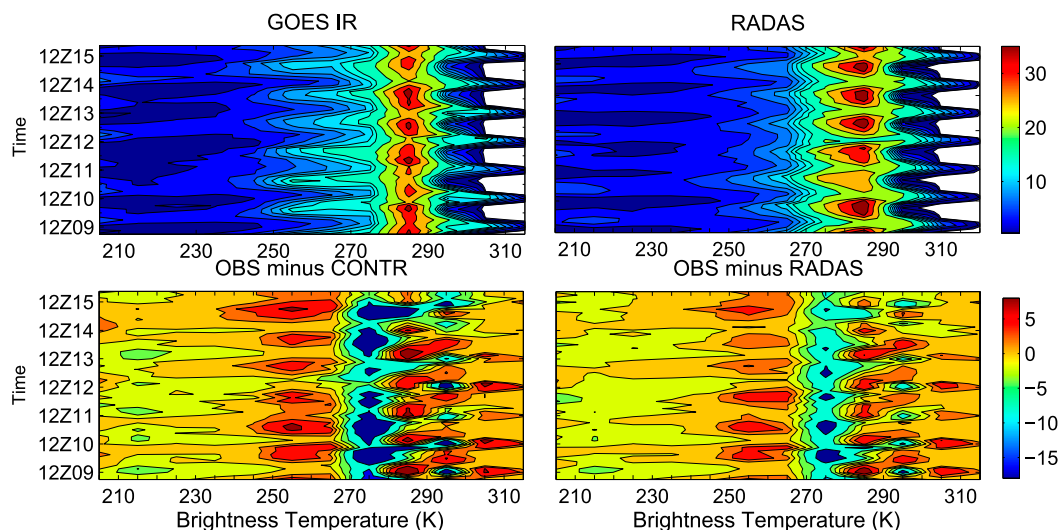


FIG. 10. The time series of infrared radiance ($T_{b11\mu m}$) histogram, depicting the diurnal cycle of cloud systems in the WAM. The data are sampled in the domain during the experiment period. (top left) Merged GOES-IR observations. (top right) Model simulations from RADAS. The bottom panels show the differences: (bottom left) observations minus CONTR and (bottom right) observations minus RADAS. The color bar represents the percentage of total counts.

diurnal cycle of land-atmosphere coupling, with an increased occurrence of lower $T_{b11\mu m}$ in the late afternoon and sustained over nighttime. Observation-simulation differences in $T_{b11\mu m}$ CFTSD show that RADAS has lower biases than CONTR, although both simulations

missed the significant diurnal variation of the mid- and low-level cloud development.

The Hovmöller diagrams of $T_{b11\mu m}$ in Fig. 11 are calculated by averaging $T_{b11\mu m}$ between the equator and 27°N in the domain at every analysis time. As

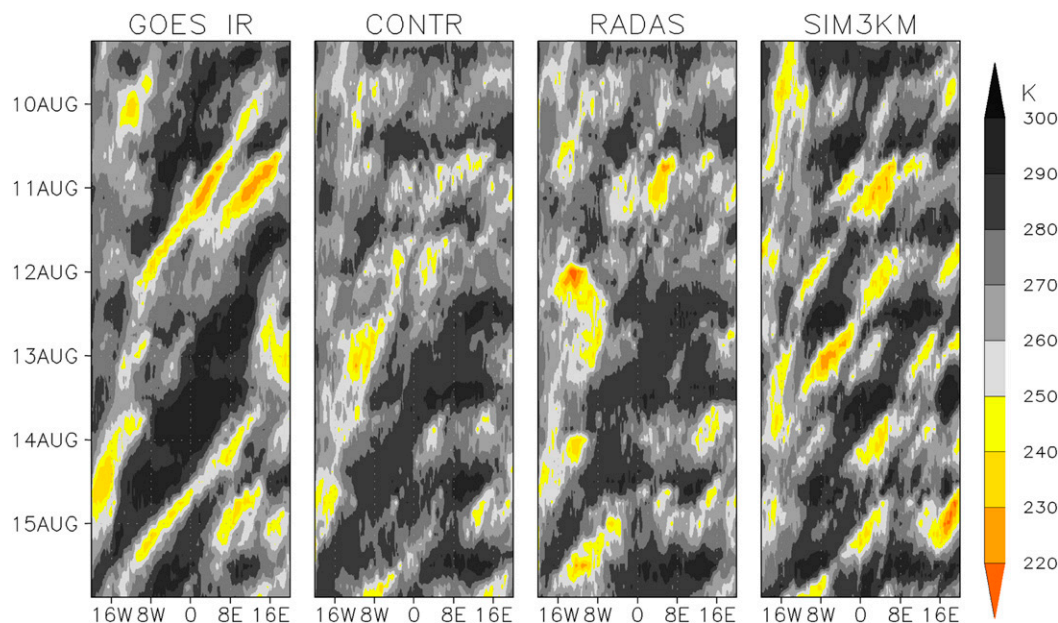


FIG. 11. The Hovmöller diagrams of infrared radiance ($T_{b11\mu m}$). The observed and simulated $T_{b11\mu m}$ are averaged between the equator and 27°N in the domain at every analysis time during the experiment period. Cold IR brightness temperatures (representing high-top cloud systems) are marked in yellow and orange. (left) Merged GOES-IR product. (right three panels) Simulated results from CONTR, RADAS, and SIMU3KM, respectively.

illustrated by the cold $Tb_{11\mu m}$ (marked in bright yellow color) in the observation panel, during the experiment a number of deep convective cloud systems initiated and propagated westward. Some of them traveled and lasted for hours, as seen around 11 and 15 August, while others stayed in the same area and were short-lived. Thus, $Tb_{11\mu m}$ Hovmöller diagrams describe the life cycle of convective systems in the WAM. Compared to the observed, cloud systems in CONTR lacked distinguishable convection features and overestimated low-level cloud cover. RADAS cloud systems benefited from the assimilation of precipitation radiances, the representation of convection systems is slightly improved. For example, a deep convection cloud system started near 5°E around 1800 UTC as observed by GOES IR. CONTR simulation only had some midlevel clouds. RADAS simulation clearly showed a deep convection developed there and propagated west at a similar phase speed as the observed. However, the improvement overall is modest. The overestimation of mid- to low-level cloud cover persists, and the convection systems that were initiated are not as deep and could not be sustained as long as the observed. This may be attributed to the systematic errors in model physics and dynamics, which data assimilation is not designed to correct. On the other hand, the model horizontal resolution (9-km grid spacing) may not be fine enough to effectively resolve propagating convection. We conducted a parallel simulation with horizontal grid spacing of 3 km, without data assimilation (SIMU3KM). Shown in Fig. 11 (the right panel) the cloud systems from this simulation have substantially increased propagation of convective clouds, although the frequency of occurrence may be overestimated. RADAS (9KM) improves the convective system strength relative to CONTR, but no substantial impact on the frequency of occurrence. If the burden of computation cost is eased in the future, we expect that a combination of finer model resolution and all-sky radiance data assimilation can significantly improve the model simulation of convective systems in West Africa monsoon.

The vertical structure of cloud profiles can be evaluated using the *CloudSat* CPR observations (cloudsat.cira.colostate.edu). CPR is a W-band (94 GHz) radar for profiling cloud and light precipitation processes (Tanelli et al. 2008). Direct backscatter signals from CPR 94-GHz attenuating radar reflectivity (dBZ_{m94GHz}) are used for evaluating the distributions of cloud-precipitation profiles over the experiment domain. We selected 28 *CloudSat* overpasses during the experiment period. Cloud-precipitation masks are created for each echo profile, when CPR echoes exceed the minimum significant threshold (-28 dBZ). Zonal cloud

frequencies are then derived in the area from the equator to 27°N. Figure 12 shows the highest frequencies of all-level clouds between 6° and 10°N, indicating the location of ITCZ during the period. Cirrus cloud outflows are captured in surrounding regions of the ITCZ. High frequencies of low-level signals below 2 km between the equator to 5°N suggest a presence of marine low clouds. High frequencies of midlevel clouds are stretched in the zone between 14° and 27°N.

Radar simulator in G-SDSU is used to simulate CPR attenuating dBZ_{m94GHz} (Matsui et al. 2014). Similar to microwave and visible-IR simulator, the simulation uses prescribed parameters consistent with that of the model microphysics, including hydrometeor types, phase, particle size distributions, and effective density. A T-matrix single scattering database (Liao et al. 2013) is applied in the simulation of dBZ_{m94GHz} . The simulated CPR echo profiles are collocated in space and in time to the observed 28 *CloudSat* swaths. Using the same approach as we used for observations, we construct the zonal frequencies of cloud-precipitation profiles from the simulations based on experimental results of CONTR, RADAS, and SIMU3KM.

Both RADAS and CONTR capture general structure of the cloud vertical profiles, but low cloud fraction between the equator and 12°N is overestimated, while the mid- and high-level clouds, especially in the ITCZ zone, are underestimated, compared to the *CloudSat* observation. According to the observed, the deep clouds deck is located at or about 10 km in height, reaching heights of 14–15 km. Note that the underestimation of high clouds often affects the radar signals at lower levels due to severe attenuation in W-band radar. SIMU3KM has fewer aforementioned biases and with deep convection occasionally reaching 14-km height. The higher model resolution of SIMU3KM reduces slightly the low cloud biases, and midlevel cloud frequencies are increased around the ITCZ zone. Midlevel clouds are underestimated in northern regions. Because *CloudSat* CPR is an on-nadir radar profiler with very limited sampling path, the location of cloud systems is critical in developing the zonal map shown here, especially in a relative short sampling period. Thus, model biases shown here may reveal the contribution of sampling errors as well. Additional forward simulations are conducted with randomly changed *CloudSat* orbiting passes to investigate the impact of sampling errors. The result indicates very small change in overall patterns of the zonal frequencies (not shown here).

d. Impact on thermodynamic interaction

The assimilation of precipitation-sensitive radiances introduces observation-based constraint to model

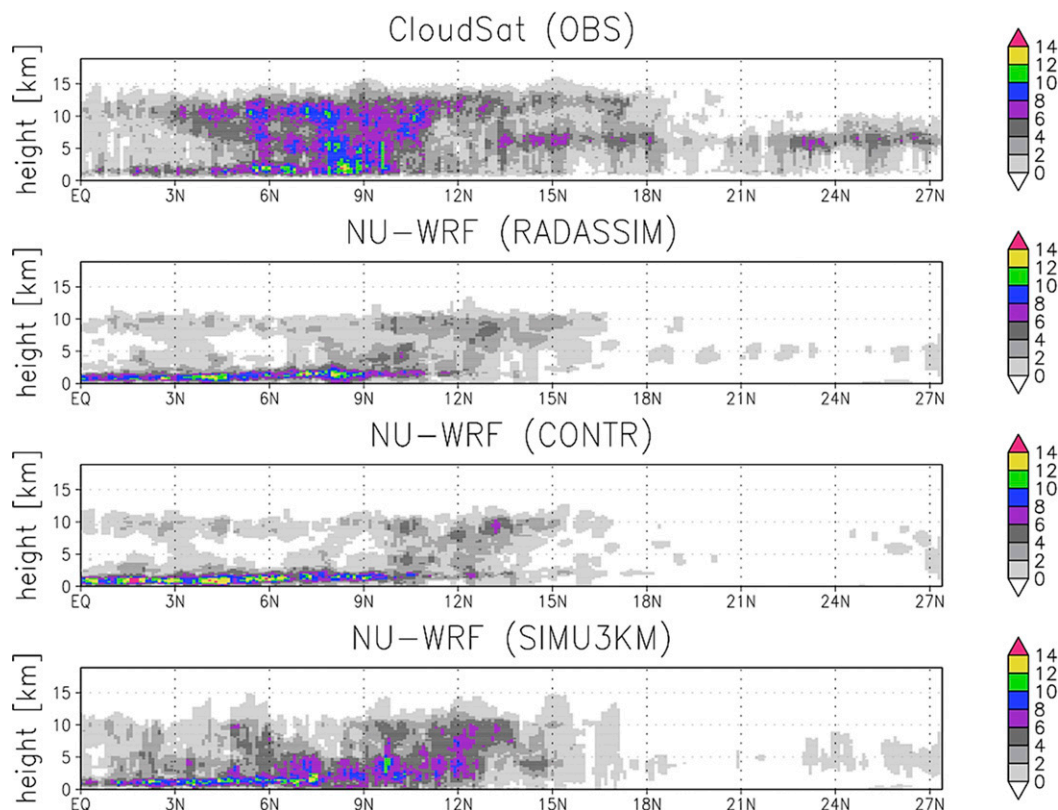


FIG. 12. Zonal frequency of cloud mask derived from *CloudSat* CPR observations and simulations of CONTR, RADAS, and SIMU3KM. The cloud masks are created for each echo profile when CPR echoes exceed the threshold (-28 dBZ).

precipitation processes that interact with dynamics. Because of the interaction and feedback, the changes in model physical processes brought by the assimilation may induce a profound modification of the atmospheric thermodynamic structure in the WAM, one of the most meteorologically sensitive regions in the world (McCrary et al. 2014; Reale et al. 2014). For instance, any change in the low- to midtroposphere thermal structure in the region could affect the AEJ and the low-level monsoonal flow, or influence the pattern of moisture flux transport and convergence. In this section we examine the changes in the thermodynamic fields of short-term forecasts in CONTR and RADAS induced by the assimilation and assess the data impact on dynamic interaction in the WAM simulation.

Temperature and humidity fields are directly related to cloud precipitation processes, and winds interact with physical processes through thermodynamics. The radiance data impact on these variables can be realized via cross-variable error covariance in the analysis procedure and through dynamic interaction during the model integration. Table 2 shows the error statistics of short-term forecast fits to available conventional observations,

sampled from 3-h forecasts (issued from CONTR and RADAS) at observation locations and times. The temperature, moisture, and wind observation departures are calculated to obtain observation-minus-forecast root-mean-square errors. The verification shows that precipitation radiance assimilation has modest but consistent positive impact on moisture and zonal wind, but the impacts on temperature and meridional wind are not statistically significant.

Frequently occurring precipitation processes in the atmosphere in the WAM interact with the moisture transport in spatial and temporal scales often larger than that of precipitation. The lower-level moisture flow originates predominately from the Atlantic Ocean. The northern propagation of the monsoonal flow brings

TABLE 2. Root-mean-square errors of short-term 3-h forecasts minus conventional data, sampled at observation locations and times. The values in parentheses are the number of samples.

Experiment	T (K)	Q (g kg^{-1})	U (m s^{-1})	V (m s^{-1})
CONTR	1.57 (4104)	1.56 (1513)	5.38 (4749)	4.68 (4749)
RADAS	1.55	1.49	4.35	4.08

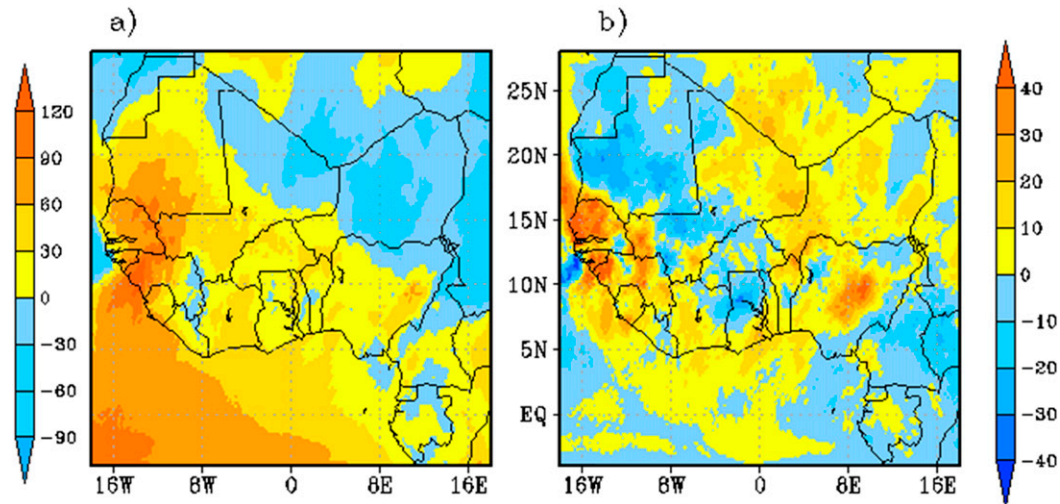


FIG. 13. Time-mean meridional moisture transport vertically integrated from the surface to 600 hPa (in $\text{kg m}^{-1} \text{s}^{-1}$): (a) the result from RADAS, and (b) the difference (RADAS minus CONTR).

moisture from the oceanic area toward the continent to the precipitation band. To examine the impact caused by the precipitation radiance data assimilation in RADAS on the moisture transport with respect to CONTR, the mean moisture transport is computed during the experiment period. Figure 13 shows the time-mean meridional moisture transport vertically integrated from the surface to 600 hPa. As illustrated in Fig. 13a, the moisture source for the monsoon precipitation is predominantly from offshore of Guinea coast. The large-scale transport of moisture in the lower levels of troposphere retains the moisture on the way and feeds into precipitation band. The moisture transport is particularly concentrated in the areas corresponding to the maxima of precipitation, one in the west coast region of Guinea and Senegal with an offshore extension, the other in the region of Adamawa highlands in Nigeria. The difference of moisture transport structures between two experiments shown in Fig. 13b indicates that the northward meridional moisture flux to the Guinea coastal area is increased significantly as a consequence of precipitation radiance assimilation. There is also a spatial pattern modification manifested by the dipole feature just offshore of Guinea, indicating a localized eastward shift of the moisture transport from sea to the land.

The Saharan heat low (SHL) represents a unique thermodynamic feature of the WAM. The SHL is another indicator of the characteristics of the monsoon meridional circulation important for moisture transport in the WAM. The changes in monsoon precipitation can influence the structure and strength of the SHL depending on the relative north–south pressure gradient. Figure 14 shows the

geopotential height anomalies in latitude–height cross section, averaged between 15°W and 15°E and averaged in time. The SHL with combined effect of low pressure and high temperature is represented by negative geopotential height anomalies near the surface. In RADAS analysis the SHL is centered at 19°N with negative geopotential height anomalies up to the 800-hPa level. Above the SHL the geopotential height anomalies become positive, representing high pressure corresponding to the lifting of the isobaric surfaces over the heat source. At low levels, the large-scale pressure gradient between the Gulf of Guinea and the Sahara is a critical mechanism to drive monsoon circulation. Simulations from both experiments capture this large-scale thermodynamic feature. The difference is small. It is mostly shown in the position of the maximum and low-pressure extension to the south.

The AEJ is a very important dynamical component of the WAM. During summer the contrast between the cool moist ocean and hot dry desert creates strong gradients of temperature and moisture, the jet develops at around 600 hPa. Figure 15 shows the time-averaged zonal wind at 600 hPa and at meridional–height cross section (averaged between 15°W and 10°E). The strength of AEJ is not impacted much by the assimilation, with the maximum speed of 14 m s^{-1} in CONTR and RADAS. The difference map indicates that near the southern edge the jet has a steeper meridional gradient in RADAS comparing to that in CONTR. The difference in the meridional–height cross section shows that the southern boundary AEJ is shifted northward as affected by the precipitation data assimilation. The low-level zonal wind is not affected in terms of the maximum and its location in CONTR and RADAS.

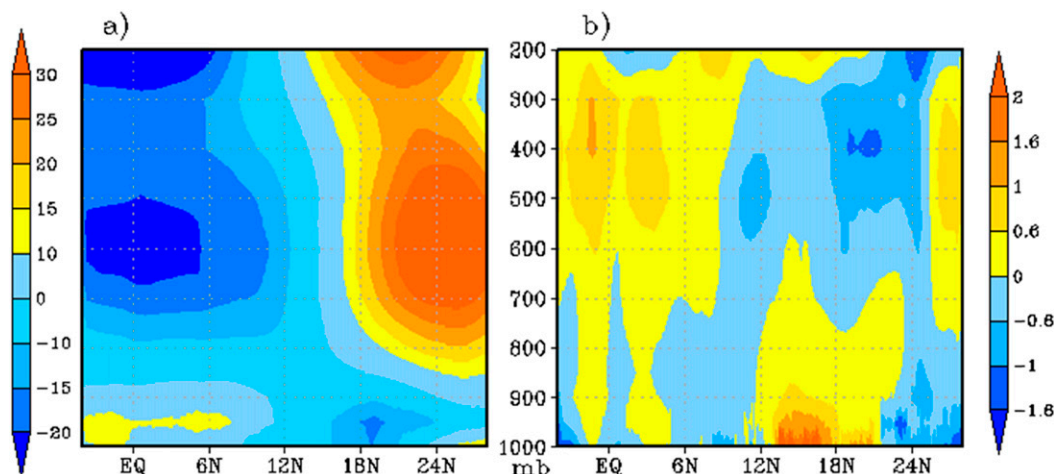


FIG. 14. Saharan heat low (SHL) represented by the time-mean geopotential height anomalies (in m). The results are shown in height-meridional cross section, averaged between 15°W and 15°E: (a) the RADAS result, and (b) the difference (RADAS minus CONTR).

5. Conclusions

We applied an ensemble-based data assimilation methodology to the assimilation of spaceborne precipitation-sensitive radiance observations in the NU-WRF simulation

of the WAM. The data impact is assessed using independent observations on precipitation and cloud systems in the atmosphere, surface precipitation, and the interaction and feedback with wind, temperature, and moisture. The use of satellite-observed precipitation information via direct

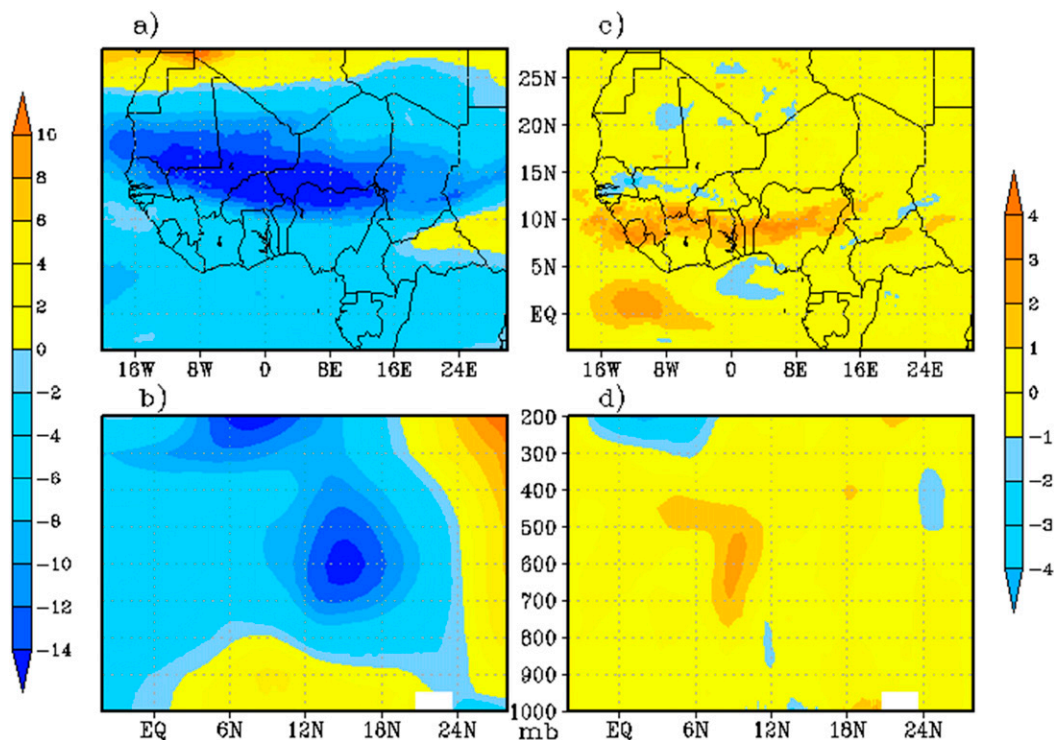


FIG. 15. Time-mean zonal wind (in m s^{-1}) depicting the African easterly jet (AEJ). (a) Mean zonal wind at 600 hPa from RADAS. (b) Mean zonal wind from RADAS in height-meridional cross section, averaged between 15°W and 10°E. (c),(d) The differences between RADAS and CONTR, at 600 hPa and in height-meridional cross section, respectively.

radiance assimilation improves the overall representation of cloud and precipitation processes in the NU-WRF simulation of the WAM.

The analysis consists of the full description of atmospheric states and a realistic cloud and precipitation distribution that is consistent with the observed dynamic and physical features of the WAM. The analysis shows an improved representation of monsoon precipitation and its interaction with dynamics over West Africa. Most significantly, assimilation of precipitation-sensitive microwave radiance has a positive impact on the distribution of precipitation intensity and modulates the propagation of cloud precipitation systems associated with AEJ. Using an ensemble-based assimilation technique that allows state-dependent forecast error covariance among dynamical and microphysical variables, the assimilation of radiances over the WAM rainband provides better hydrometeor distributions for storm initiation with characteristics of continental tropical convection, although fundamental model biases associated with insufficient model resolution remains unresolved issue in NU-WRF EDAS, as revealed by geostationary and *CloudSat* satellites.

It has been a challenging issue in precipitation data assimilation to retain cloud and precipitation derived from analysis in the forecast, because it mainly depends on the model microphysics parameterizations that govern the cloud and precipitation processes in subsequent forecasts. For the example of the storm in Fig. 4, the impact of the precipitation-sensitive radiances on the analyses of hydrometeors is significant. The subsequent 3-h forecast initiated from that analysis produced more intense rainfall in the storm region with a local maximum of 55-mm accumulation in 3 h, a substantial improvement over the forecast without radiance assimilation. The similar results of precipitation forecasts with and without radiance assimilation are illustrated in the case shown in Fig. 6. The short-term precipitation forecast initialized from radiance assimilation has higher correlation with the observed brightness temperature depression. Some broader features of the monsoon precipitation are improved by the radiance assimilation such as the zonal mean distribution and the magnitude of late afternoon rain rates in regional diurnal cycle, as shown in Fig. 7. On the other hand, some “short memory” responses of model physics in subsequent forecasts are also observed for instance in Figs. 11 and 12, particularly in cloud fields. Figure 11 (along with Fig. 5) shows that although the analyses were improved by precipitating radiances, there were still situations in which the radiances did not impact the forecast for the better. Data assimilation systems are still a long way from successfully fitting most cloud and

precipitation feature that is observed in the radiances. These results also indicate that the influence of analysis increments on clouds in model forecast is highly state dependent. In previous studies of assimilating all-sky radiances in the North American midlatitudes (Zhang et al. 2013), it has been observed that negative increments (removing precipitation clouds) tend to remain effective while positive ones (generating precipitation clouds) may dissipate in short time depending on the model physics and the environment. In this study of West African tropical region, dissipation happens more often on convection systems that have been created by the analysis. Furthermore, model resolution plays an important role as well. The convective cloud system occurrence in the region is impacted more by a finer model resolution than radiance data. Comparing the results to cloud observations GOES IR as in Fig. 11, and to *CloudSat* as in Fig. 12, we observe that the finer resolution SIMU3KM simulates convective systems more frequently than the observed, while radiance assimilation RADAS (9-km resolution) improves the convective system strength relative to that in CONTR, but has less impact on the frequency of occurrence. If the burden of computation cost is eased in the future, we expect that a combination of finer model resolution and radiance data assimilation can significantly improve the model simulation of convective systems in West Africa monsoon.

The experiments of this study cover a relative short time period during the WAM, mainly because ensemble data assimilation experiments at high-resolution are computationally intensive. The findings in the current one-week period experiments are encouraging and instructive, more robust verifications will need experiments with longer period covering multiple monsoon seasons in the future. While a conclusive statement on the data impact at seasonal and climate scales cannot be made at this stage, evidence is provided by this study that radiance observation information in presence of clouds and precipitation could be a critical contribution to improve the WAM simulation in terms of precipitation and thermodynamic interaction and to advance our understanding of the mechanism and process in the evolution of the WAM.

Acknowledgments. This work is supported by the NASA Global Precipitation Measurement mission and Earth Science Enterprise’s Modeling and Analysis Program. Computations were carried out at NASA Advanced Supercomputing (NAS). Authors thank Eric Kemp, Jossy Jacob, and Erich Stocker at NASA Goddard Space Flight Center for their assistance with software support and data processing.

REFERENCES

- Aires, F., C. Prigent, F. Bernardo, C. Jiménez, R. Saunders, and P. Brunel, 2011: A Tool to Estimate Land-Surface Emissivities at Microwave Frequencies (TELSEM) for use in numerical weather prediction. *Quart. J. Roy. Meteor. Soc.*, **137**, 690–699, doi:[10.1002/qj.803](https://doi.org/10.1002/qj.803).
- Bosilovich, M. G., F. R. Robertson, and J. Chen, 2011: Global energy and water budgets in MERRA. *J. Climate*, **24**, 5721–5739, doi:[10.1175/2011JCLI4175.1](https://doi.org/10.1175/2011JCLI4175.1).
- Chambon, P., S. Q. Zhang, A. Y. Hou, M. Zupanski, and S. H. Cheung, 2014: Assessing the impact of pre-GPM microwave precipitation observations in the Goddard WRF ensemble data assimilation system. *Quart. J. Roy. Meteor. Soc.*, **140**, 1219–1235, doi:[10.1002/qj.2215](https://doi.org/10.1002/qj.2215).
- Chou, M.-D., and M. J. Suarez, 1999: A solar radiation parameterization for atmospheric studies. NASA Tech. Rep. NASA/TM-1999-104606, Vol. 15, 38 pp.
- , and —, 2001: A thermal infrared radiation parameterization for atmospheric studies. NASA Tech. Rep. NASA/TM-2001-104606, Vol. 19, 55 pp.
- Ebert, E. E., 2008: Fuzzy verification of high-resolution forecasts: A review and proposed framework. *Meteor. Appl.*, **15**, 51–64, doi:[10.1002/met.25](https://doi.org/10.1002/met.25).
- Geer, A. J., and P. Bauer, 2011: Observation errors in all-sky data assimilation. *Quart. J. Roy. Meteor. Soc.*, **137**, 2024–2037, doi:[10.1002/qj.830](https://doi.org/10.1002/qj.830).
- , —, and P. Lopez, 2010: Direct 4D-Var assimilation of all-sky radiances. Part II: Assessment. *Quart. J. Roy. Meteor. Soc.*, **136**, 1886–1905, doi:[10.1002/qj.681](https://doi.org/10.1002/qj.681).
- Gelaro, R., and Coauthors, 2017: The Modern-Era Retrospective Analysis for Research and Applications, version 2 (MERRA-2). *J. Climate*, **30**, 5419–5454, doi:[10.1175/JCLI-D-16-0758.1](https://doi.org/10.1175/JCLI-D-16-0758.1).
- Giannini, A., M. Biasutti, I. M. Held, and A. H. Sobel, 2008: A global perspective on African climate. *Climatic Change*, **90**, 359–383, doi:[10.1007/s10584-008-9396-y](https://doi.org/10.1007/s10584-008-9396-y).
- Grell, G. A., and D. Devenyi, 2002: A generalized approach to parameterizing convection combining ensemble and data assimilation techniques. *Geophys. Res. Lett.*, **29**, 1693, doi:[10.1029/2002GL015311](https://doi.org/10.1029/2002GL015311).
- Hou, A. Y., and Coauthors, 2014: The Global Precipitation Measurement Mission. *Bull. Amer. Meteor. Soc.*, **95**, 701–722, doi:[10.1175/BAMS-D-13-00164.1](https://doi.org/10.1175/BAMS-D-13-00164.1).
- Huffman, G. J., and Coauthors, 2007: The TRMM Multisatellite Precipitation Analysis: Quasi-global, multi-year, combined-sensor precipitation estimates at fine scale. *J. Hydrometeorol.*, **8**, 38–55, doi:[10.1175/JHM560.1](https://doi.org/10.1175/JHM560.1).
- Janowiak, J. E., R. J. Joyce, and Y. Yarosh, 2001: A real-time global half-hourly pixel-resolution infrared dataset and its applications. *Bull. Amer. Meteor. Soc.*, **82**, 205–217, doi:[10.1175/1520-0477\(2001\)082<0205:ARTGHH>2.3.CO;2](https://doi.org/10.1175/1520-0477(2001)082<0205:ARTGHH>2.3.CO;2).
- Kidd, C. K., D. R. Kniveton, M. C. Todd, and T. J. Bellerby, 2003: Satellite rainfall estimation using combined passive microwave and infrared algorithms. *J. Hydrometeorol.*, **4**, 1088–1104, doi:[10.1175/1525-7541\(2003\)004<1088:SREUCP>2.0.CO;2](https://doi.org/10.1175/1525-7541(2003)004<1088:SREUCP>2.0.CO;2).
- Kiladis, G. N., C. D. Thorncroft, and N. M. J. Hall, 2006: Three-dimensional structure and dynamics of African easterly waves. Part I: Observations. *J. Atmos. Sci.*, **63**, 2212–2230, doi:[10.1175/JAS3741.1](https://doi.org/10.1175/JAS3741.1).
- Kumar, S. V., C. D. Peters-Lidard, J. L. Eastman, and W.-K. Tao, 2008: An integrated high-resolution hydrometeorological modeling testbed using LIS and WRF. *Environ. Modell. Software*, **23**, 169–181, doi:[10.1016/j.envsoft.2007.05.012](https://doi.org/10.1016/j.envsoft.2007.05.012).
- Kummerow, C., and Coauthors, 2001: The evolution of the Goddard Profiling Algorithm (GPROF) for rainfall estimation from passive microwave sensors. *J. Appl. Meteor.*, **40**, 1801–1820, doi:[10.1175/1520-0450\(2001\)040<1801:TEOTGP>2.0.CO;2](https://doi.org/10.1175/1520-0450(2001)040<1801:TEOTGP>2.0.CO;2).
- Lang, S. E., W.-K. Tao, X. Zeng, and Y. Li, 2011: Reducing the biases in simulated radar reflectivities from a bulk microphysics scheme: Tropical convective systems. *J. Atmos. Sci.*, **68**, 2306–2320, doi:[10.1175/JAS-D-10-05000.1](https://doi.org/10.1175/JAS-D-10-05000.1).
- Liao, L., R. Meneghini, H. K. Nowell, and G. Liu, 2013: Scattering computations of snow aggregates from simple geometrical particle models. *IEEE J. Sel. Top. Appl. Earth Obs. Remote Sens.*, **6**, 1409–1417, doi:[10.1109/JSTARS.2013.2255262](https://doi.org/10.1109/JSTARS.2013.2255262).
- Matsui, T., X. Zeng, W.-K. Tao, H. Masunaga, W. Olson, and S. Lang, 2009: Evaluation of long-term cloud-resolving model simulations using satellite radiance observations and multi-frequency satellite simulators. *J. Atmos. Oceanic Technol.*, **26**, 1261–1274, doi:[10.1175/2008JTECHA1168.1](https://doi.org/10.1175/2008JTECHA1168.1).
- , and Coauthors, 2013: GPM satellite simulator over ground validation sites. *Bull. Amer. Meteor. Soc.*, **94**, 1653–1660, doi:[10.1175/BAMS-D-12-00160.1](https://doi.org/10.1175/BAMS-D-12-00160.1).
- , and Coauthors, 2014: Introducing multisensor satellite radiance-based evaluation for regional Earth system modeling. *J. Geophys. Res. Atmos.*, **119**, 8450–8475, doi:[10.1002/2013JD021424](https://doi.org/10.1002/2013JD021424).
- McCrary, R. R., D. A. Randall, and C. Stan, 2014: Simulations of the West African monsoon with a superparameterized climate model. Part I: The seasonal cycle. *J. Climate*, **27**, 8303–8322, doi:[10.1175/JCLI-D-13-00676.1](https://doi.org/10.1175/JCLI-D-13-00676.1).
- Mounier, F., G. N. Kiladis, and S. Janicot, 2007: Analysis of the dominant mode of convectively coupled Kelvin waves in the West African monsoon. *J. Climate*, **20**, 1487–1503, doi:[10.1175/JCLI4059.1](https://doi.org/10.1175/JCLI4059.1).
- Nakajima, T., and M. Tanaka, 1986: Matrix formulations for the transfer of solar radiation in a plane-parallel scattering atmosphere. *J. Quant. Spectrosc. Radiat. Transfer*, **35**, 13–21, doi:[10.1016/0022-4073\(86\)90088-9](https://doi.org/10.1016/0022-4073(86)90088-9).
- , and —, 1988: Algorithms for radiative intensity calculations in moderately thick atmospheres using a truncation approximation. *J. Quant. Spectrosc. Radiat. Transfer*, **40**, 51–69, doi:[10.1016/0022-4073\(88\)90031-3](https://doi.org/10.1016/0022-4073(88)90031-3).
- Olson, W. S., and Coauthors, 2006: Precipitation and latent heating distributions from satellite passive microwave radiometry. Part I: Improved method and uncertainties. *J. Appl. Meteor. Climatol.*, **45**, 702–720, doi:[10.1175/JAM2369.1](https://doi.org/10.1175/JAM2369.1).
- , and Coauthors, 2016: The microwave radiative properties of falling snow derived from nonspherical ice particle models. Part II: Initial testing using radar, radiometer and in situ observations. *J. Appl. Meteor. Climatol.*, **55**, 709–722, doi:[10.1175/JAMC-D-15-0131.1](https://doi.org/10.1175/JAMC-D-15-0131.1).
- Peters-Lidard, C. D., and Coauthors, 2007: High-performance Earth system modeling with NASA/GSFC's Land Information System. *Innov. Syst. Software Eng.*, **3**, 157–165, doi:[10.1007/s11334-007-0028-x](https://doi.org/10.1007/s11334-007-0028-x).
- , and Coauthors, 2015: Integrated modeling of aerosol, cloud, precipitation and land processes at satellite-resolved scales. *Environ. Modell. Software*, **67**, 149–159, doi:[10.1016/j.envsoft.2015.01.007](https://doi.org/10.1016/j.envsoft.2015.01.007).
- Reale, O., K. M. Lau, and A. da Silva, 2011: Impact of interactive aerosol on the African easterly jet in the NASA GEOS-5 global forecasting system. *Wea. Forecasting*, **26**, 504–519, doi:[10.1175/WAF-D-10-05025.1](https://doi.org/10.1175/WAF-D-10-05025.1).

- , —, —, and T. Matsui, 2014: Impact of assimilated and interactive aerosol on tropical cyclogenesis. *Geophys. Res. Lett.*, **41**, 3282–3288, doi:[10.1002/2014GL059918](https://doi.org/10.1002/2014GL059918).
- Redelsperger, J., C. D. Thorncroft, A. Diedhiou, T. Lebel, D. Parker, and J. Polcher, 2006: African Monsoon Multidisciplinary Analysis: An international research project and field campaign. *Bull. Amer. Meteor. Soc.*, **87**, 1739–1746, doi:[10.1175/BAMS-87-12-1739](https://doi.org/10.1175/BAMS-87-12-1739).
- Reichle, R. H., 2012: The MERRA-Land Data Product. GMAO Office Note No. 3 (version 1.2), 38 pp.
- Roberts, N. M., and H. W. Lean, 2008: Scale-selective verification of rainfall accumulations from high-resolution forecasts of convective events. *Mon. Wea. Rev.*, **136**, 78–97, doi:[10.1175/2007MWR2123.1](https://doi.org/10.1175/2007MWR2123.1).
- Roca, R., J. Lafore, C. Piriou, and J. Redelsperger, 2005: Extratropical dry-air intrusions into the West African monsoon midtroposphere: An important factor for the convective activity over the Sahel. *J. Atmos. Sci.*, **62**, 390–407, doi:[10.1175/JAS-3366.1](https://doi.org/10.1175/JAS-3366.1).
- , P. Chambon, I. Jobard, P. Kirstetter, M. Gosset, and J. C. Bergès, 2010: Comparing satellite and surface rainfall products over West Africa at meteorologically relevant scales during the AMMA campaign using error estimates. *J. Appl. Meteor. Climatol.*, **49**, 715–731, doi:[10.1175/2009JAMC2318.1](https://doi.org/10.1175/2009JAMC2318.1).
- Rodgers, C. D., 2000: *Inverse Methods for Atmospheric Sounding: Theory and Practice*. World Scientific, 238 pp.
- Roehrig, R., D. Bouniol, F. Guichard, F. Hourdin, and J.-L. Redelsperger, 2013: The present and future of the West African monsoon: A process-oriented assessment of CMIP5 simulations along the AMMA transect. *J. Climate*, **26**, 6471–6505, doi:[10.1175/JCLI-D-12-00505.1](https://doi.org/10.1175/JCLI-D-12-00505.1).
- Seemann, W. S., E. E. Borbas, R. O. Knuteson, G. R. Stephen, and H.-L. Huang, 2008: Development of a global infrared land surface emissivity database for application to clear sky sounding retrievals from multispectral satellite radiance measurements. *J. Appl. Meteor. Climatol.*, **47**, 108–123, doi:[10.1175/2007JAMC1590.1](https://doi.org/10.1175/2007JAMC1590.1).
- Simpson, J., C. Kummerow, W.-K. Tao, and R. F. Adler, 1996: On the Tropical Rainfall Measuring Mission (TRMM). *Meteor. Atmos. Phys.*, **60**, 19–36, doi:[10.1007/BF01029783](https://doi.org/10.1007/BF01029783).
- Skamarock, W. C., and Coauthors, 2008: A description of the Advanced Research WRF version 3. NCAR Tech. Note NCAR/TN-475+STR, 113 pp., doi:[10.5065/D68S4MVH](https://doi.org/10.5065/D68S4MVH).
- Skinner, C. B., and N. S. Diffenbaugh, 2013: The contribution of African easterly waves to monsoon precipitation in the CMIP3 ensemble. *J. Geophys. Res. Atmos.*, **118**, 3590–3609, doi:[10.1002/jgrd.50363](https://doi.org/10.1002/jgrd.50363).
- Tanelli, S., S. Durden, E. Im, K. S. Pak, D. G. Reinke, P. Partain, J. Haynes, and R. Marchand, 2008: CloudSat's Cloud Profiling Radar after two years in orbit: Performance, calibration, and processing. *IEEE Trans. Geosci. Remote Sens.*, **46**, 3560–3573, doi:[10.1109/TGRS.2008.2002030](https://doi.org/10.1109/TGRS.2008.2002030).
- Wilheit, T., C. Kummerow, and R. Ferraro, 2003: Rainfall algorithms for AMSR-E. *IEEE Trans. Geosci. Remote Sens.*, **41**, 204–213, doi:[10.1109/TGRS.2002.808312](https://doi.org/10.1109/TGRS.2002.808312).
- Wu, M.-L., O. Reale, S. Schubert, M. J. Suarez, R. Koster, and P. Pegion, 2009: African easterly jet: Structure and maintenance. *J. Climate*, **22**, 4459–4480, doi:[10.1175/2009JCLI2584.1](https://doi.org/10.1175/2009JCLI2584.1).
- Yang, S.-C., E. Kalnay, B. Hunt, and N. E. Bowler, 2009: Weight interpolation for efficient data assimilation with the local ensemble transform Kalman filter. *Quart. J. Roy. Meteor. Soc.*, **135**, 251–262, doi:[10.1002/qj.353](https://doi.org/10.1002/qj.353).
- Zhang, S. Q., M. Zupanski, A. Y. Hou, X. Lin, and S. H. Cheung, 2013: Assimilation of precipitation-affected radiances in a cloud-resolving WRF ensemble data assimilation system. *Mon. Wea. Rev.*, **141**, 754–772, doi:[10.1175/MWR-D-12-00055.1](https://doi.org/10.1175/MWR-D-12-00055.1).
- Zupanski, D., A. Y. Hou, S. Q. Zhang, M. Zupanski, C. Kummerow, and S. H. Cheung, 2007: Applications of information theory in ensemble data assimilation. *Quart. J. Roy. Meteor. Soc.*, **133**, 1533–1545, doi:[10.1002/qj.123](https://doi.org/10.1002/qj.123).
- Zupanski, M., 2005: Maximum likelihood ensemble filter: Theoretical aspects. *Mon. Wea. Rev.*, **133**, 1710–1726, doi:[10.1175/MWR2946.1](https://doi.org/10.1175/MWR2946.1).